Characterization and Adsorption Mechanism of Methylene Blue Dye by Mesoporous Activated Carbon Prepared from Rice Husks

Suchada Sawasdee* and Prachart Watcharabundit

Faculty of Science and Technology, Thepsatri Rajabhat University, Lop Buri 15000, Thailand

ARTICLE INFO

Received: 2 Mar 2023
Received in revised: 7 Jul 2023
Accepted: 14 Jul 2023
Published online: 21 Sep 2023
DOI: 10.32526/ennrj/21/20230074

Keywords:
Adsorption/ Activated carbon/ Rice husks/ Methylene blue/ Mesopore

*** Corresponding author:**
E-mail: ps_neng@hotmail.com

ABSTRACT

Environmental contamination due to synthetic dyes is a severe problem due to their adverse eco-toxicological effects. This study prepared activated carbon from H_3PO_4-activated rice husks (AC-RH) to adsorb methylene blue (MB) and predicted the adsorption mechanism. The AC-RH was characterized for N_2 adsorption, surface functional groups, chemical compositions, and surface morphology. The activated carbon was classified to be a mesoporous material because 87% of its pore volume diameters are 3-50 nm. MB adsorption was studied under different conditions. Optimal MB adsorption occurred at pH 8, and the ideal equilibrium time was 360 min. The equilibrium adsorption was evaluated at concentrations of MB between 25 and 200 mg/L at 30°C. The Freundlich isotherm model matched the equilibrium data, and the greatest adsorption capacity of the Langmuir isotherm was 26.31 mg/g. The kinetic analysis revealed that the adsorption was pseudo-second-order, and its rate constant (k_2) was higher at higher temperatures. For the thermodynamic adsorption study at 20 to 40°C, the Gibbs free energy (ΔG) values were -6.291 to -9.197 kJ/mol, and the activation energy (E_a) was 26.248 kJ/mol: therefore, the methylene blue adsorption was spontaneous and physical. This study also revealed that the adsorption mechanisms were H-bonding, pore-filling, Yoshida H-bonding, n-π interactions, electrostatic, and cation exchange.

1. INTRODUCTION

Synthetic dyes are employed in the textile industry, including pulp mills, paper, printing, plastics, foods, and leather, and dye molecules degrade poorly in response to light, heat, and chemicals (Han et al., 2012). Most dyes are toxic and cause serious difficulties for the ecological system; water contaminated with dye harms aquatic life. Methylene blue (MB), a cationic dye, is often used for coloring and dyeing and is found in high concentrations in industrial effluent (Patawat et al., 2020). MB is a stable molecule that is not readily biodegradable (Hu et al., 2017), and it can cause health problems, including increased heart rate, vomiting, shock, cyanosis, mental confusion, eye burns, tissue necrosis, headache, nausea, and chest discomfort (Uner et al., 2016). Various treatment methods have been utilized for dye removal in effluents, and adsorption is widely used to treat dyes from wastewater since it is a low-cost process with excellent efficiency (Uner et al., 2016).

An activated carbon (AC) adsorbent can be utilized in water treatment because its surface area is large, and the functional groups that exist on its surfaces lead to a significant interaction in the adsorptive capacities of activated carbons (Kumar and Jena, 2016; Jawad et al., 2017). Commercial activated carbon is expensive and hard to reuse; hence, AC should be produced from cheap, readily available materials. Several investigations (Zazouli et al., 2016; Patawat et al., 2020; Han et al., 2020) have been conducted to search for activated carbons prepared from agricultural by-products or waste.

Rice husks are agricultural waste, and their residues are abundant in Thailand, ~7.5×10^9 kg per year (Wantaneeyakul et al., 2021). The main components of rice husks are organic matter (70-85%) and mineral components (20-30%), such as silica,

Citation: Sawasdee S, Watcharabundit P. Characterization and adsorption mechanism of methylene blue dye by mesoporous activated carbon prepared from rice husks. Environ. Nat. Resour. J. 2023;21(5):458-470. (https://doi.org/10.32526/ennrj/21/20230074)

alkalis, and trace elements (Hossain et al., 2018). Shrestha et al. (2019) have used NaOH, $ZnCl_2$, and KOH to create nanoporous carbon material from rice husks, whereas Sharma and Uma (2010) have carbonized rice husks for 2 h at 650°C with a nitrogen flow of 150 mL/min to adsorb MB dye. Phosphoric acid (H_3PO_4) treatment, according to Al-Asadi et al. (2023), might increase the ability of activated carbon produced from fig leaves to adsorb MB from aqueous solutions, when compared to other activating agents, such as NaOH and H_2SO_4. No study has discussed the adsorption mechanism of rice husk-activated carbon and MB. This work generated activated carbon from rice husks (AC-RH) using H_3PO_4 as an activator, which was subsequently used to adsorb MB, and the adsorption mechanism was explained. The AC was characterized using N_2 adsorption, surface functional groups, chemical compositions, and surface morphology. The adsorption variables were investigated for the highest adsorption, and the data obtained were analyzed using the isotherm and kinetic models. Also, thermodynamic adsorption was evaluated in order to calculate the Gibbs free energy (ΔG), enthalpy (ΔH), and entropy (ΔS). The overall results were used to confirm the adsorption mechanism.

2. METHODOLOGY

2.1 Material preparations

The rice husks employed in this investigation originated at a rice mill in Lopburi, Thailand. The rice husks were oven-dried at 80°C after being cleaned with distilled water. The dried rice husks were soaked in 1.0 mol/L H_3PO_4 at a ratio of 1/20 (g/mL) for a day. They were then oven-dried at 100°C. At 500°C for 1 h, the dried char was carbonized. It was then rinsed thoroughly with water that had been distilled until its pH value was neutral. The AC was dried and ground into powder. Then, it was sieved to 150-300 µm particle size. It was dried and kept in a desiccator for use as the adsorbent.

MB (CI 52015, $C_{16}H_{18}N_3SCl$, Merck, Germany, M.W. 319.98 g/mol) was used as the adsorbate. By diluting a 1,000 mg/L stock solution with distilled water, working solutions of MB (25-200 mg/L) were obtained. The MB solution was adjusted to the required pH (OHAUS Starter 5000, USA.) by adding hydrochloric acid (0.1 M) or sodium hydroxide (0.1 M). The analytical-grade phosphoric acid (H_3PO_4), sodium hydroxide (NaOH), and hydrochloric acid (HCl) were purchased from Merck and Co.

2.2 Characterization of adsorbent

The N_2 adsorption of the adsorbent was determined using a gas sorption analyzer (Autosorb 1 MP, Quantachrome Instruments, USA), and the adsorption data was used to determine the Brunauer-Emmett-Teller (BET) surface area and Barrett-Joyner-Halenda (BJH) pore size distribution. The surface functional groups, chemical compositions, and surface morphology were analyzed using Fourier transform infrared (FTIR) spectroscopy (Model two, Perkin Elmer, USA), X-ray fluorescence (XRF) spectrometry (MESA-500W, HORIBA, Japan), X-ray diffraction (XRD) spectrometry (Smartlab2, Rigaku Japan), and scanning electron microscopy (SEM, 1450 VP LEO, Leo, UK).

The pH at the point of zero charges, pH_{pzc}, was determined using the pH drift method. A series of 0.1 M KNO_3 solutions were prepared with pH values between 2 and 12. The solution pH was adjusted by adding 0.1 M HCl and 0.1 M NaOH and measured using a pH meter. Then, 0.1 g of adsorbent was added for every 100 mL of 0.1 M KNO_3 solution, and the mixtures were shaken at 150 rpm for 48 h. Each mixture was filtered, and its pH was measured. The pH_{pzc} was calculated by plotting the curve of each ΔpH (pH_{final}-$pH_{initial}$) against $pH_{initial}$. The pH_{pzc} is when the curve (ΔpH vs. $pH_{initial}$) meets the line ΔpH=0.

2.3 Adsorption studies

During the batch adsorption test, the suspended combination of 100 mL of dye solution and 0.6 g of adsorbent was placed into a series of 250-mL Erlenmeyer flasks. The adsorption experiments were conducted at pH 2-10, contact time of 1-540 min, initial dye concentrations of 25-200 mg/L, and temperatures between 20-40°C. The suspended sample in each flask was shaken at 200 rpm. After the sample was filtered at the appointed time, the amount of dye still present in the solution was measured using an UV-visible spectrophotometer (Specord 210 plus, Analytik Jena, Germany) operating at a wavelength of 665 nm. The adsorption capacity (q_t) was determined as follows:

$$q_t = (C_o - C_t)\ V/M \quad (1)$$

Where; C_o (mg/L) and C_t (mg/L) are the concentration of MB dye at initial and any time, respectively; V (L) is the volume of MB dye solution; q_t (mg/g) is the adsorption capacity at any time; and W (g) is the mass of the adsorbent. All the adsorption

experiments were performed in triplicate, and the average adsorption capacity values were used for data analysis.

The adsorption data were analyzed using the linear forms of the pseudo-first-order, pseudo-second-order kinetic, and intraparticle diffusion kinetic models, which are Equations. (2), (3), and (4), respectively.

$$\log(q_e - q_t) = \log q_e - k_1 t/2.303 \quad (2)$$

$$t/q_t = (1/k_2 q_e^2) + t/q_e \quad (3)$$

$$q_e = K_{id}(t)^{1/2} + C \quad (4)$$

Where; k_1 (1/min) and k_2 (g/mg/min) are the rate constant of the pseudo-first-order and pseudo-second-order models, respectively, K_{id} (mg/g/min$^{1/2}$) is the intraparticle diffusion constant, and C (mg/g) is the intercept representing the thickness of the external diffusion layer. Also, q_e (mg/g) is the adsorption capacity at equilibrium.

The adsorption data at equilibrium were analyzed using the non-linear forms of the Langmuir, Freundlich, and Redlich-Peterson isotherm models, which are presented in Equations (5), (6), and (7), respectively:

$$q_e = q_{max} K_L C_e/(1 + C_e K_L) \quad (5)$$

$$q_e = K_F C_e^{1/n} \quad (6)$$

$$q_e = A C_e/(1 + B C_e^g) \quad (7)$$

Where; q_e (mg/g) is the equilibrium adsorption capacity; C_e (mg/L) is the equilibrium concentration of adsorbate; K_L (L/mg) is the Langmuir constant; and q_{max} (mg/g) is the maximum adsorption capacity. For the Freundlich isotherm, K_F (L/g) is the adsorption capacity and 1/n is the adsorption intensity. A (L/g) and B (L/mg) are the Redlich-Peterson isotherm constants, and g is an exponent between 0 and 1. As stated in Equation (8), we calculated the non-linear coefficient of determination (R^2) to assess the fit of an isotherm model to the experimental data (Islam et al., 2015).

$$R^2 = 1 - \frac{\sum_{N=1}^{N}(q_{e.exp} - q_{e.mod})^2}{\sum_{N=1}^{N}(q_{e.exp} - \overline{q_{e.exp}})^2} \quad (8)$$

Where; N is the number of experimental data, $q_{e.exp}$ and $q_{e.mod}$ are the experimental and isotherm model-predicted adsorption capacities at equilibrium, respectively. Further, $q_{\overline{e.exp}}$ is the average of $q_{e.exp}$.

2.4 Adsorption thermodynamics

The adsorption thermodynamics explains the energy change and the mechanism involved in the adsorption process. According to Equation (9), the Gibbs free energy (ΔG) is related to the equilibrium constant, K_c(K_c=q_e/C_e). The linear curve is given by the plot of ln K_c versus 1/T in Equation (10). The enthalpy (ΔH) and entropy (ΔS) can be calculated using the slope and intercept of the plot, respectively.

$$\Delta G = -RT \ln K_c \quad (9)$$

$$\ln K_c = (\Delta S/R) - \Delta H/RT \quad (10)$$

Where; R (8.314 J/mol/K) is the gas constant and T (K) is the absolute temperature.

3. RESULTS AND DISCUSSION

3.1 Characterization of adsorbent

3.1.1 Brunauer-Emmett-Teller (BET) and Barrett-Joyner-Halenda (BJH) analysis

Following the IUPAC classification, the AC-RH N_2 adsorption-desorption isotherm in this study was Type IV(a) (Cychosz and Thommes, 2018). The isotherm showed hysteresis caused by capillary condensation in the mesopores. A Type IV isotherm indicates the existence of mesopores in the adsorbent and the formation of a multilayer structure at low pressure (Jawad et al., 2017). The N_2 adsorption isotherm data were used to determine BET surface area and BJH pore size distribution. The parameters of the BET and BJH analyses are provided in Table 1.

Table 1. Surface area and pore size distribution of AC-RH

Parameters	Values
BET surface area (m^2/g)	244.479
BET total pore volume (cm^3/g)	0.142
BET average pore diameter (nm)	2.324
BET average pore radius (nm)	1.165
BJH pore volume (cm^3/g)	0.025
BJH average pore diameter (nm)	3.701
BJH average pore radius (nm)	1.805

The BET-specific surface area of the adsorbent was 244.479 m^2/g, with a total pore volume of 0.142 cm^3/g and an average pore diameter of 2.324 nm. The

BJH pore size distributions shown in Figure 1 indicated that the average pore diameter was 3.701 nm; the adsorbent was mesoporous. Moreover, the pore diameter distribution was between 3.11 and 136.28 nm, indicating that the AC-RH consisted of mesopores (2-50 nm) and a few macropores (>50 nm). About 87% of the pore volume had pore diameters between 3 and 50 nm, and the pores with a diameter >50 nm comprised about 13% of the total. Because the MB size (0.59-1.38 nm) (Thang et al., 2021) is smaller than the pore size, it can enter and adsorb in the pores of the AC-RH.

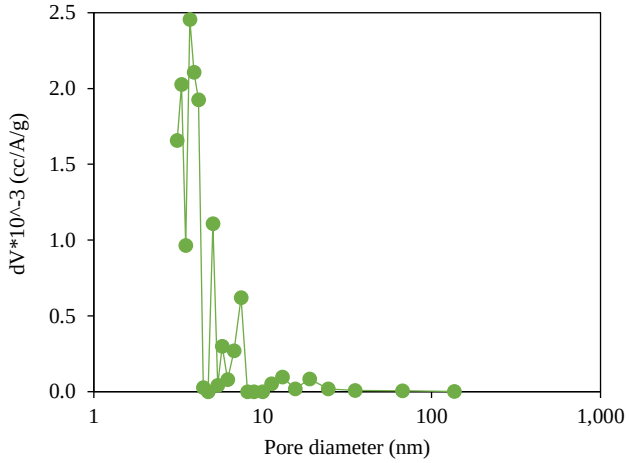

Figure 1. Pore size distribution of activated carbon from H_3PO_4-activated rice husks (AC-RH)

3.1.2 X-ray fluorescence (XRF) analysis

The chemical compositions of the AC-RH adsorbent before and after dye adsorption were investigated by XRF. The main elements present in the adsorbent were Si (45.71%), K (28.85%), Fe (11.97%), and Ca (9.515%). After dye adsorption, the amounts of Si and K were reduced to 41.90% and 27.80%, respectively. The decreased amount of K indicated that cationic exchange plays a role in MB adsorption on the AC-RH surface (Zhu et al., 2018).

3.1.3 X-ray diffraction (XRD) analysis

The XRD patterns of AC-RH before and after dye adsorption are shown in Figure 2. Figure 2(a) shows the XRD patterns of the AC before the adsorption between 2θ of 10° and 60°. The broad diffraction peaks at around 15°-30° indicated that the AC was amorphous (Ziezio et al., 2020), whereas sharp peaks indicate crystalline material (El-Bindary et al., 2021). Diffraction peaks were observed at 27.7°, 28.0°, 30.0°, 31.2°, 42.8°, and 51.3°, with an estimated average crystallite size of 76.8 nm determined by using the Scherrer equation. Also, the broad band at around 22° was attributed to amorphous silica (Wazir et al., 2020). The low intensity of the peak at around 43° showed the graphite structure and disorder formed by the activated carbon (Serafin et al., 2023). Moreover, these peaks at around 43° are associated with the honeycomb structure of sp^2 hybridized carbon, indicating that the sample was formed of turbostratic carbon (Banuprabha et al., 2021). The diffraction peaks after adsorption (Figure 2(b)) appeared at 21.9°, 23.7°, 27.6°, 28.0°, 29.6°, 30.2°, 33.6°, 35.4°, 51.3°, 62.4°, 67.7°, and 69.5°. Figure 2(b) shows that the peak intensity changed, with some peaks disappearing and others reappearing, suggesting that the AC had become saturated with MB (Unugul and Nigiz, 2020).

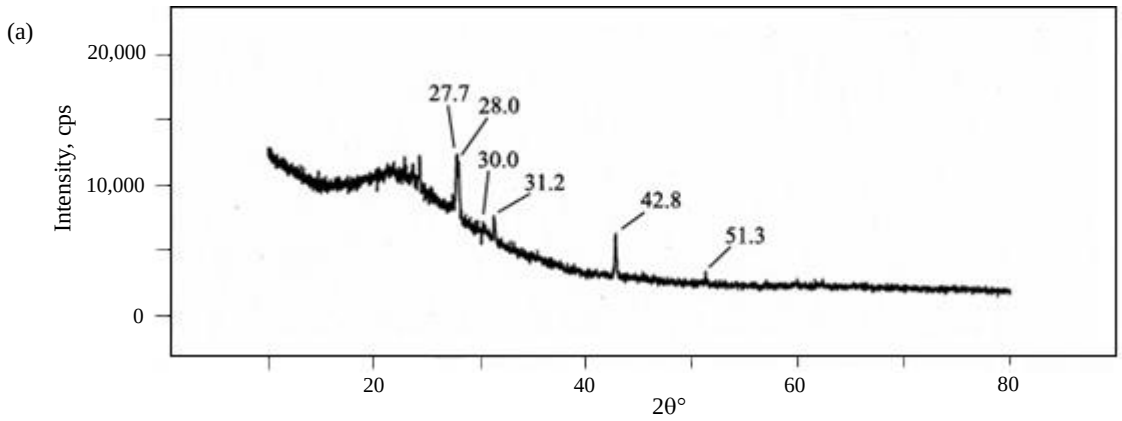

Figure 2. X-ray diffraction (XRD) patterns of AC-RH (a) before and (b) after adsorption

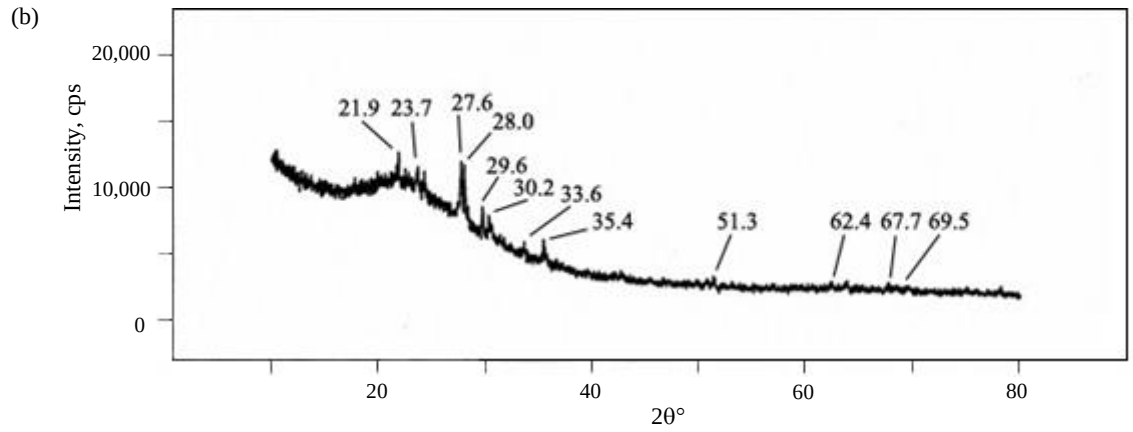

Figure 2. X-ray diffraction (XRD) patterns of AC-RH (a) before and (b) after adsorption (cont.)

3.1.4 Determination of pH at point of zero charges (pH_{pzc})

The pH_{pzc} of the AC-RH was analyzed by the pH drift method, as shown in Figure 3, and the pH_{pzc} was 5.2. When the pH is lower than pH_{pzc}, the surface charge of the adsorbent is positively charged ($\Delta pH>0$). When the pH is higher than pH_{pzc}, the surface charge of the adsorbent is negatively charged ($\Delta pH<0$), and an electrostatic attraction might form between the negatively charged surface and the cationic MB dye molecules. This suggests that MB adsorption on AC is more efficient at a pH higher than 5.2.

3.1.5 Scanning electron microscopy (SEM) analysis

The SEM images of the adsorbent are shown in Figure 4(a, b, and c). The raw rice husks showed a roughly structured fibrous material without pores. In contrast, the SEM image of AC-RH (Figure 4(b)) shows a porous structure. The acid broke down the glycosidic bonds in the cellulose and the aryl bonds in the lignin (Yakout and El-Deen, 2016), forming pores in the adsorbent. At the same time, the silica remained in the rice husk (Ahiduzzaman and Sadrul Islam, 2016). Figure 4(c) shows the surface of AC-RH after MB adsorption coated with MB dye, with no pores visible.

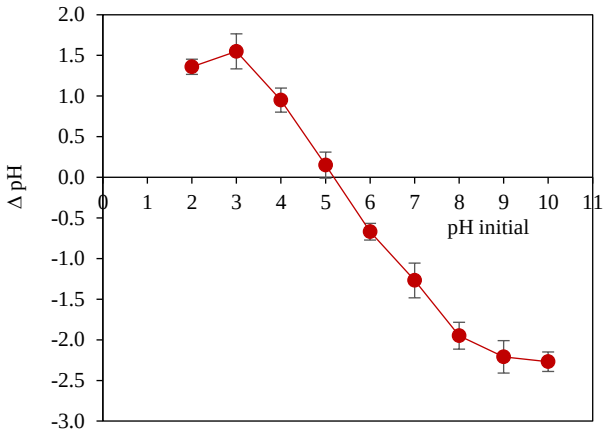

Figure 3. pH_{pzc} of adsorbent

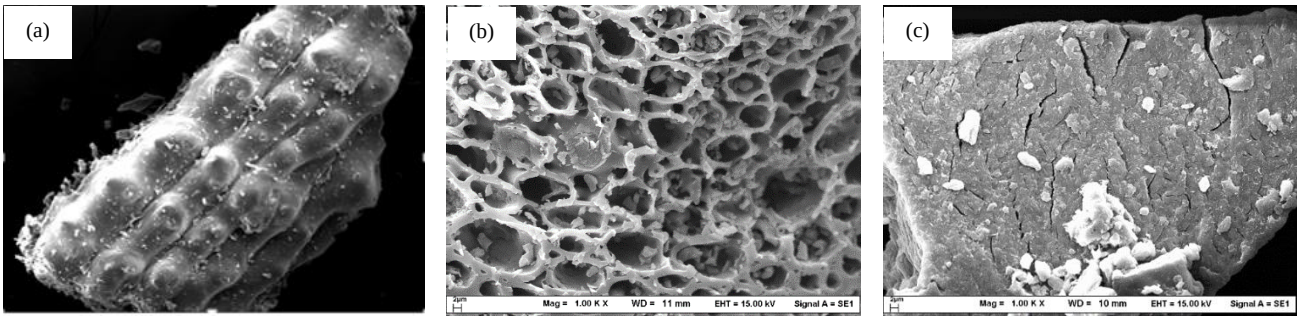

Figure 4. SEM images of AC-RH (a) raw rice husk, (b) before adsorption, and (c) after adsorption

3.1.6 Fourier transform infrared (FTIR) spectroscopy analysis

Figure 5(a, b) shows the FTIR spectra of the AC-RH surface. The broad absorption peak observed prior to adsorption between 3,300 and 3,600 cm^{-1}, peaking at 3,452 cm^{-1}, was ascribed to the OH stretching vibration (Figure 5(a)) (Jawad et al., 2017). According to Al-Ghouti and Al-Absi (2020), the peak

at 1,750 cm^{-1} can be attributed to the stretching vibration of the C=O functional group. According to Liu et al. (2020), the aromatic ring C=C stretching vibration in the AC appeared at 1,596 cm^{-1}. The band at 1,217 cm^{-1} was attributed to the Si-O-Si vibration in amorphous SiO_2 (Hongo et al., 2021). According to Puziy et al. (2002) and İzgi et al. (2018), the peaks between 1,000 and 1,200 cm^{-1} correspond to the O-C bond in carboxylic acids, alcohols, phenols, and esters. The bands at 500-800 cm^{-1} were attributed to the C-H bending mode of out-of-plane aromatic ring deformation (Alau et al., 2015). According to Bakdash et al. (2020), the peak at 789 cm^{-1} is linked to the Si-O-C stretching vibration. Therefore, the AC-RH used in this study contained OH, COOH, C=O, C=C, and Si-O-Si functional groups.

After adsorption, the peaks shifted (Figure 5(b)), and their intensities differed from the original spectrum. For example, the peak at 1,596 cm^{-1} shifted to 1,595 cm^{-1} with an increased intensity due to dye adsorption. Also, the intensities of the Si-O-C and Si-O-Si peaks at 789 and 1,217 cm^{-1} weakened during adsorption due to n-π interactions between the lone pair of O (Si-O) and π-electrons in the MB molecule (Zhu et al., 2018). Moreover, new peaks appeared at 3,359 and 3,237 (stretching vibration of OH group), 2,815 ($-N(CH_3)_3$), 1,656 ($=N^+$ immonium band), 1,357 and 1,342 (C-N), 1,038 (heterocycle skeleton), and 876 cm^{-1} (C-H bending in heterocyclic) (Amin et al., 2017), showing the adsorption of the MB onto the AC-RH.

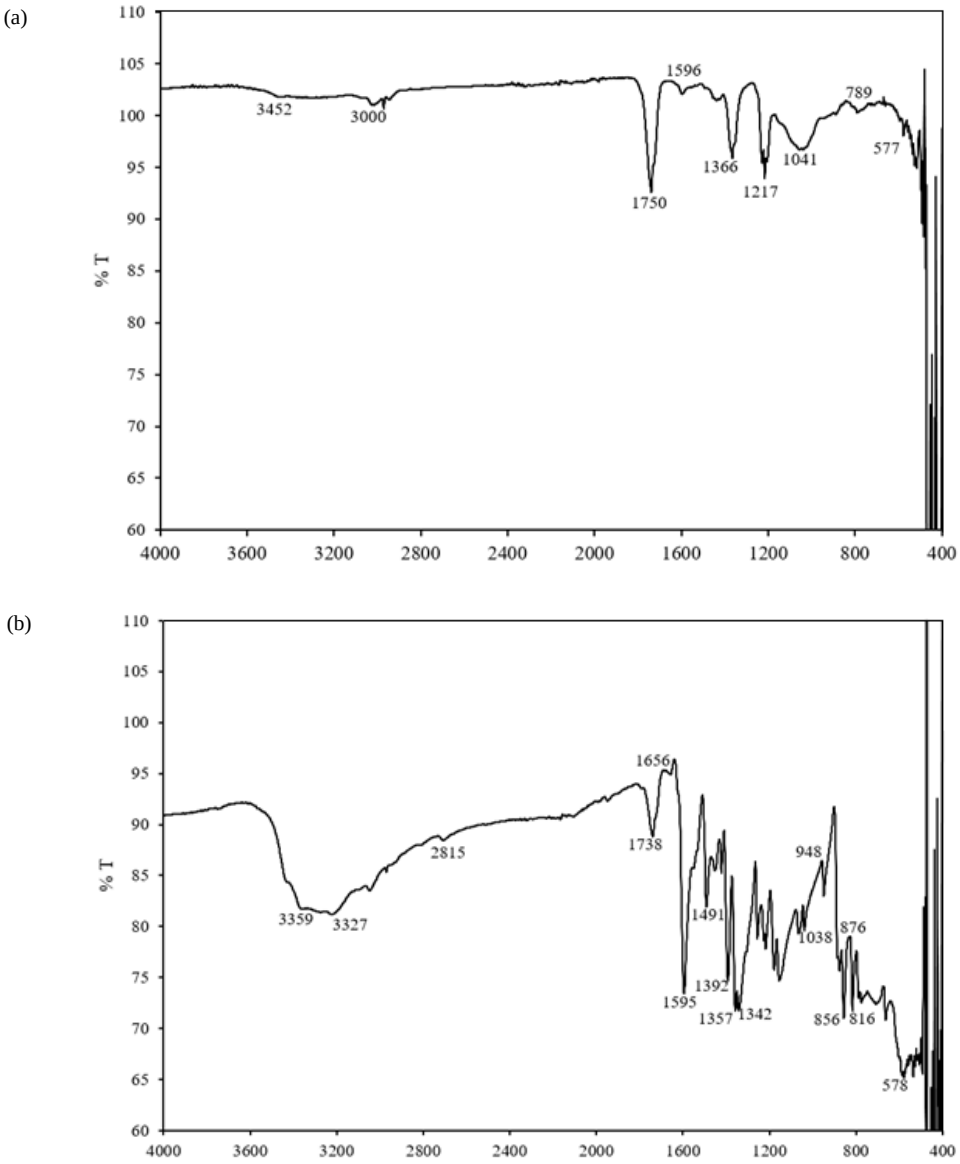

Figure 5. FTIR spectra of adsorbent (a) before and (b) after adsorption

3.2 Effect of pH on adsorption

Figure 6 shows the effects of pH (2-10) on the adsorption. As seen in Figure 6, the adsorption capacity was enhanced when the pH was increased from 2 to 8, and the optimal removal was determined at pH 8. At a pH greater than 8, the adsorption capacity did not change significantly. When the pH of the dye solution was low, the surface charge of the adsorbent became positive, repelling the positive dye molecules.

At a pH greater than 5.2 (pH_{pzc}), the surface of the adsorbent was negative (Equation 11), driving an electrostatic attraction between the cationic dye (MB^+) and the negative surface of the adsorbent ($R\text{-}O^-$), as seen in Equation (12). This observation was consistent with other reports (Zazouli et al., 2016; Pathania et al., 2017) of MB adsorption onto AC from different sources.

$$R - OH + HO^- \rightarrow R - O^- + H_2O \quad (11)$$

$$R - O^- + MB^+ \rightarrow R - O^-MB^+ \quad (12)$$

3.3 Effect of contact time and temperature

Figure 7 shows the contact time-dependent adsorption at 1-540 min. Due to the empty adsorption sites of the adsorbent and the high dye concentration, adsorption occurred quickly during the first 15 min. After that, the adsorption rate slowly decreased until the equilibrium adsorption was reached at 360 min. This is because while the adsorption process occurred, the number of empty sites on the adsorbent and the dye concentration decreased. Mansour et al. (2021) have confirmed that the dye molecules were adsorbed on the exterior surface of the AC via boundary adsorption during the first rapid adsorption stage. A comparable report has been presented for MB adsorption by AC developed from eucalyptus residue (Han et al., 2020).

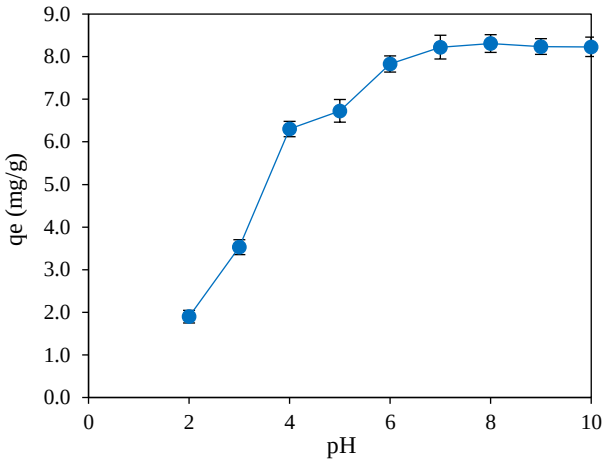

Figure 6. Effect of pH on adsorption (adsorbent dose 0.6 g, initial dye concentration 50 mg/L, contact time 360 min, and temperature 30°C)

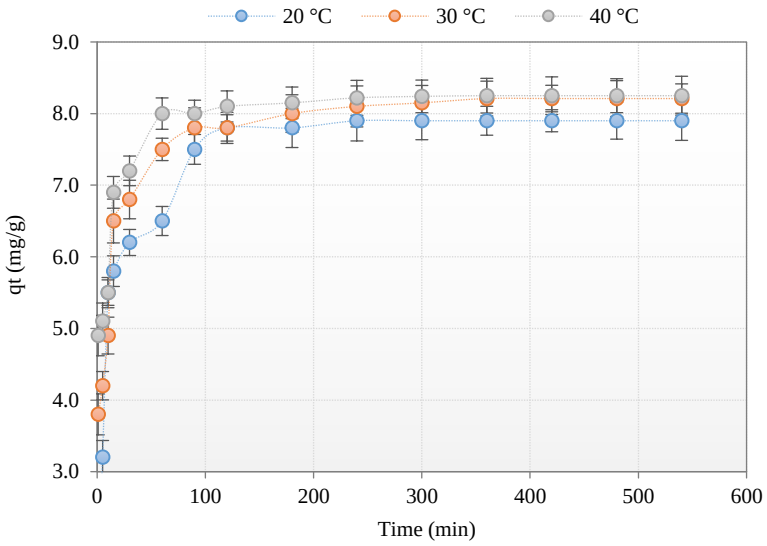

Figure 7. Effect of contact time (1, 5, 10, 15, 30, 60, 90, 120, 180, 240, 300, 360, 420, 480, and 540 min) on adsorption (adsorbent dose 0.6 g, initial dye concentration 50 mg/L, pH 8, and temperature 20-40°C)

Figure 7 also indicates that the endothermic adsorption process improved adsorption capacity as the process temperature rose from 20 to 40°C. The rise in temperature increased pore size and sorbent surface activation, boosting adsorption. In addition, increased temperature enhanced dye ion mobility and decreased swelling, allowing the dye molecules to permeate deeper into the adsorbent pores (Pathania et al., 2017). MB adsorption on activated carbons derived from *Citrullus lanatus* rinds (Uner et al., 2016) and coconut

leaves (Jawad et al., 2017) increased with temperature. However, in this study, the adsorption capacity did not change significantly at higher temperatures because of the reduced attractive force, which favored physisorption (Horsfall Jnr and Spliff, 2005). Also, Zhu et al. (2018) have studied the influence of temperature at 5, 15, 25, and 35°C and discovered that the effects of temperature on the adsorption capacities of MB on cow manure-derived biochar were reduced at temperatures between 25 and 35°C.

3.4 Adsorption kinetics

Kinetic models were employed to analyze the data from the contact time-dependent experiments. Figure 8 shows the linear graphs of the kinetic model. Table 2 shows the calculated kinetic parameters. The pseudo-second-order model exhibited higher R^2 values than the pseudo-first-order and intraparticle diffusion models. The pseudo-second-order model capacities (q_e, cal) were also closer to the experimental values (q_e, exp). The pseudo-second-order model fit the data better, showing that the adsorption of MB onto the AC-RH included the diffusion of an external liquid membrane, surface adsorption, and intraparticle diffusion (Zhu et al., 2018).

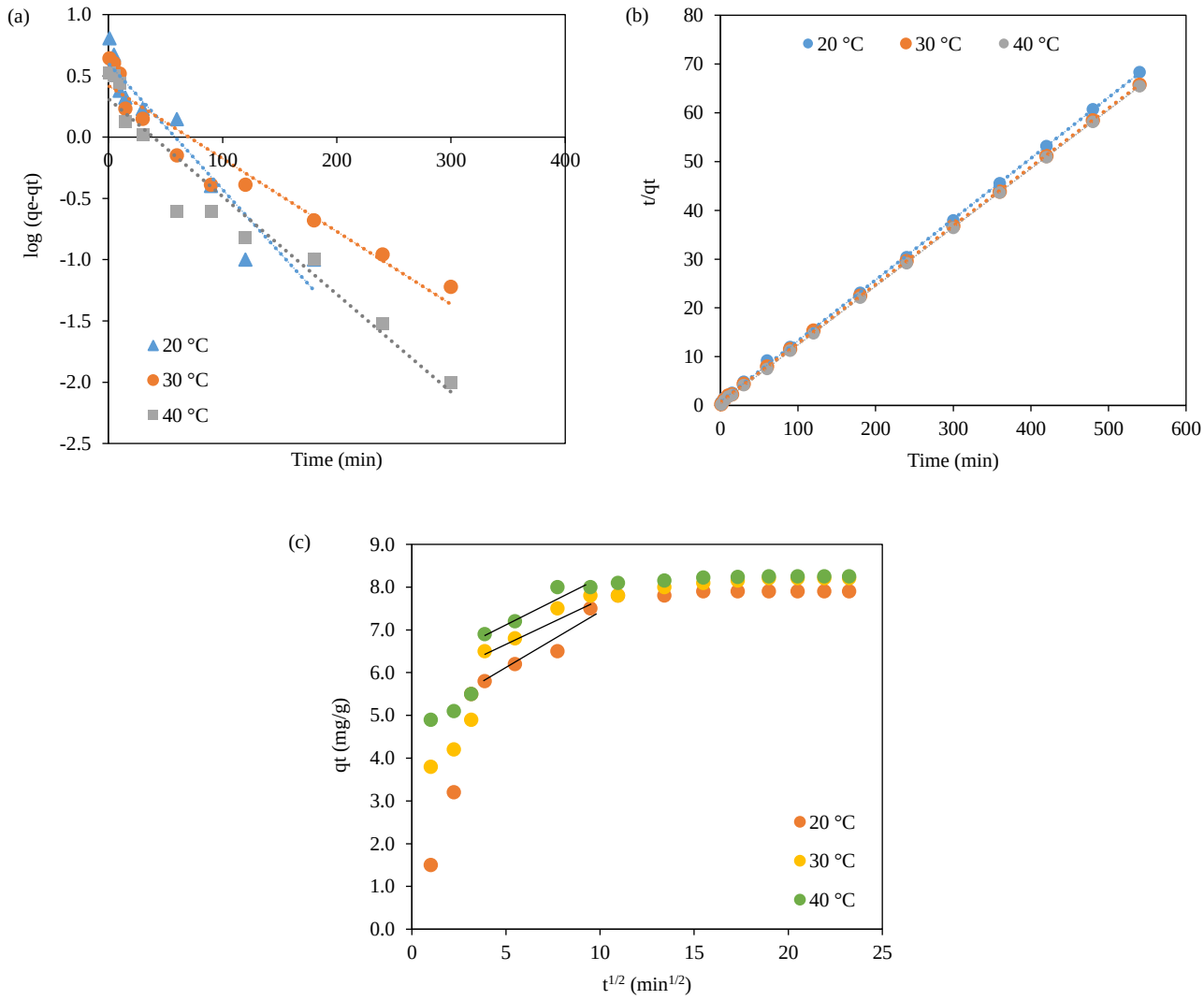

Figure 8. Kinetic models of MB adsorption: (a) pseudo-first-order, (b) pseudo-second-order, and (c) intraparticle diffusion

As seen in Figure 8(c), the plots of q_t versus $t^{1/2}$ show three stages of adsorption. In the first stage, diffusion of the boundary layer rapidly adsorbed MB molecules on the surfaces of the adsorbent. Intraparticle diffusion, the second stage, began at 15 min and lasted until 60 min. At this stage, the adsorbate was transferred from the outer surface of the adsorbent to its pores. The MB molecules were

adsorbed on the active sites of the surfaces of the adsorbent during the third step, known as the equilibrium stage (Ma et al., 2012). The second linear plot for the three temperatures had R^2 values ranging from 0.909 to 0.987. Because the line did not pass through the origin, intraparticle diffusion was not the only rate-determining step. As a result, intraparticle diffusion and external film diffusion were active during adsorption (Patawat et al., 2020). A similar observation has been reported for the adsorption of MB onto AC derived from *Citrullus lanatus* rind (Uner et al., 2016).

The activation energy (E_a) of MB adsorption onto AC-RH was determined from a plot (not shown) of ln k, the pseudo-second-order rate constant, and 1/T. The E_a value calculated from the slope of the graph was 26.248 kJ/mol. Because the E_a value was lower than 40 kJ/mol, the adsorption process of MB on AC-RH was physisorption (Inglezakis and Zorpas, 2012).

Table 2. Kinetic parameters of MB adsorption by AC-RH

Kinetic parameters	Values		
	20°C	30°C	40°C
q_e (exp) (mg/g)	7.90	8.21	8.25
Pseudo-first-order			
q_e (mg/g)	4.00	2.63	2.06
k_1 (1/min)	0.024	0.014	0.018
R^2	0.909	0.928	0.939
Pseudo-second-order			
q_e (mg/g)	8.01	8.30	8.31
k_2 (g/mg·min)	0.019	0.022	0.039
R^2	0.999	0.999	1.000
Intraparticle diffusion			
C (mg/g)	4.64	5.54	6.08
K_{id} (mg/g/min$^{1/2}$)	0.279	0.242	0.217
R^2	0.909	0.987	0.914

3.5 Adsorption isotherm

From the study of the effect of initial dye concentrations of 25-200 mg/L, the results (Figure 9) were plotted as a non-linear function between the adsorption capacity (q_e) and the equilibrium concentration of MB (C_e). Table 3 shows the adsorption isotherm parameters obtained using a non-linear solver (Excel, Microsoft). Based on the R^2, the Freundlich model, as opposed to the Redlich-Peterson and Langmuir models, provided a better description of the adsorption isotherm of MB onto AC-RH. Because the obtained 1/n value (1/n=0.231) was between 0 and 1, adsorption was favorable (Patawat et al., 2020). In addition, the Langmuir monolayer coverage (q_{max}) of MB on AC-RH was 26.31 mg/g. According to Wu et al. (2010), because the g-value for the Redlich-Peterson model was less than 1, it indicated that the adsorption was not comparable to the Langmuir isotherm model. In Table 4, the present work was compared to various research papers on MB adsorption by different ACs.

Table 3. Adsorption isotherm parameters

Isotherms	Values
Langmuir isotherm	
q_{max} (mg/g)	26.31
K_L(L/mg)	0.88
R_L	0.046-0.005
R^2	0.974
Freundlich isotherm	
K_F (L/g)	12.53
1/n	0.231
R^2	0.990
Redlich-Peterson isotherm	
A (L/g)	903.26
B (L/mg)	66.87
g	0.795
R^2	0.983

Table 4. The maximum adsorption capacity of MB on different activated carbons

Activated carbons	Optimal adsorption conditions	q_{max}(mg/g)	References
Coconut leaves	pH=5.6, 303-323°K	357.1-370.4	Jawad et al. (2017)
Bamboo	pH=6, 298°K	183.3	Liu et al. (2010)
Fig leaves	pH=7, 298°K	41.7	Al-Asadi et al. (2023)
Corn cobs	pH=8, 298°K	28.6	El-Sayed et al. (2014)
Sugarcane bagasse	pH=7, 293°K	6.7	Hazzaa and Hussein (2015)
Coconut shells	pH=8, 298°K	15.2	Khuluk et al. (2019)
Rice husks	pH=7, 303-323°K	9.8-14.3	Sharma and Uma (2010)
Rice husks	pH=8, 303°K	26.3	This study

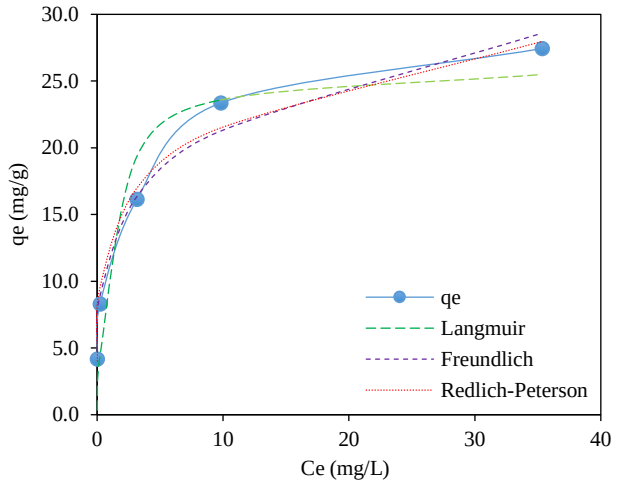

Figure 9. The equilibrium adsorption experiments and the non-linear isotherm prediction plots (initial dye concentration 25-200 mg/L, pH 8, contact time 360 min, and temperature 30°C)

3.6 Thermodynamic study

Thermodynamic equilibrium tests were conducted at 20-40°C, and the adsorption increased from 8.230 to 8.294 mg/g. Using Equation (9), the ΔG values for 20, 30, and 40°C were estimated as -6.291, -8.463, and -9.197 kJ/mol, respectively. Therefore, the adsorption was spontaneous and favorable at higher temperatures. In general, physisorption is suggested by ΔG values between -20 and 0 kJ/mol (Xu et al., 2021). Therefore, physisorption was the main mechanism involved in MB adsorption onto AC-RH.

The slope and intercept seen in Figure 10 were used to calculate ΔH and ΔS, respectively, using Equation (10). As shown by the ΔH, which was 39.565 kJ/mol, adsorption was an endothermic process. Because the ΔH value was less than 84 kJ/mol, the adsorption suggested physical sorption (Hasani et al., 2022). Because ΔS was 0.156 kJ/mol·K, it is possible that there was more randomization at the interface of the dye solution and the active sites of the adsorbent. Several other reports have also concluded that the MB adsorption on activated carbon is endothermic (Ahiduzzaman and Sadrul Islam, 2016; Pathania et al., 2017; Zazouli et al., 2016).

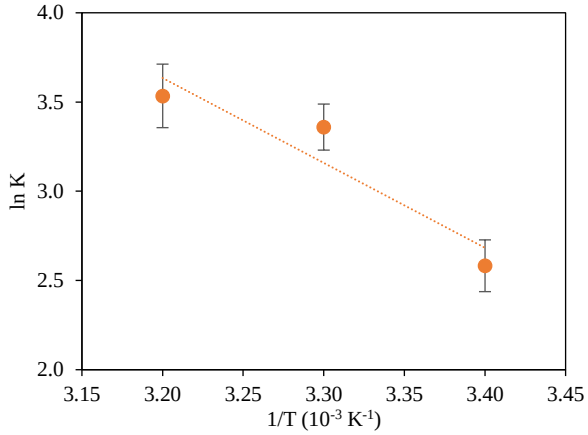

Figure 10. Thermodynamics of MB adsorption on AC-RH (initial dye concentration 50 mg/L, pH 8, and equilibrium time 360 min)

3.7 Adsorption mechanism

AC-RH surfaces contain functional groups containing oxygen atoms, called oxygen groups. These groups are important for adsorption. Additionally, the electrons (n) of the oxygen-free Lewis primary sites (electron donors) on the surfaces of AC-RH and the π-electrons of the conjugated bonds in the aromatic rings of dye molecules contributed to the adsorption interaction (Faria et al., 2004). As seen in Figure 5, the intensity of the Si-O-Si and Si-O peaks decreased after adsorption. The presence of the n-π interaction in the adsorption between the oxygen groups and dye molecules was further confirmed by the C=O peak, which lost some of its intensity and shifted from 1,750 to 1,738 cm^{-1}. The C=C peak center, on the other hand, did not shift noticeably, suggesting there were no π-π interactions (Tran et al., 2017). In addition, the C=C peak increased in intensity because of pore filling. Due to the effect of pH, an electrostatic interaction should exist between the AC-RH and the MB molecules. Therefore, the

possible mechanisms (Figure 11) of MB adsorption on AC-RH are (a) H-bonding interactions between the hydrogen on the adsorbent surface and the nitrogen in the amine group of the dye molecule; (b) pore filling in AC-RH; (c) Yoshida H-bonding interactions between the hydrogen on the OH groups in the adsorbent surface and the aromatic rings of the dye molecule; (d) n-π interactions between the oxygen functional groups of AC-RH and the aromatic rings of the dye molecule; (e) electrostatic interactions between the negatively charged AC-RH and the positively charged dye molecules (MB^+); and (f) cation exchange of MB^+ to K^+.

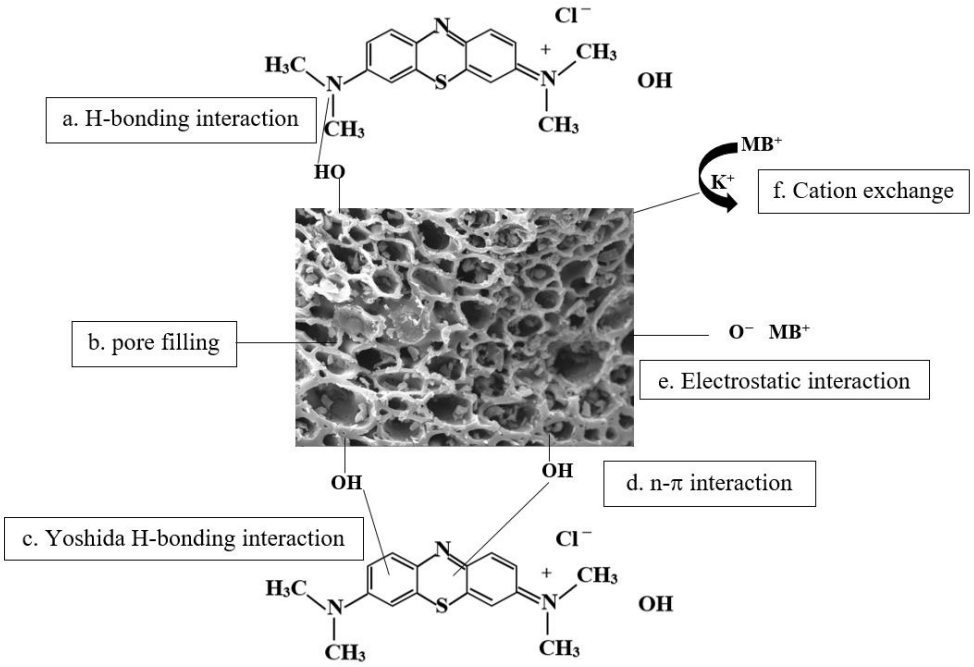

Figure 11. Possible mechanisms of MB dye adsorption on AC-RH

4. CONCLUSION

The N_2 adsorption-desorption isotherm, XRF spectroscopy, XRD, SEM, and FTIR spectroscopy were used to evaluate the pores and surfaces of AC-RH. The nitrogen adsorption-desorption isotherm was Type IV and primarily mesoporous. The BET surface area was 244.479 m^2/g. The BJH-determined pore diameter distribution ranged between 3.11 and 136.28 nm, with 87% in the 3-50 nm range. MB adsorption onto AC-RH was studied at different pH, contact times, initial dye concentrations, and temperatures. The equilibrium time was 360 min, and the highest MB adsorption occurred at pH 8. The adsorption kinetic data corresponded to the pseudo-second-order model, and the equilibrium data fit the Freundlich isotherm. According to thermodynamics models and the activation energy, the process was spontaneous, endothermic, and physisorption. The MB adsorption on AC-RH was also attributed to H-bonding, Yoshida H-bonding, pore filling, n-π interactions, cation exchange, and electrostatic attraction.

ACKNOWLEDGEMENTS

The authors would like to express their gratitude to Thepsatri Rajabhat University for the support of the research.

REFERENCES

Ahiduzzaman Md, Sadrul Islam AKM. Preparation of porous biochar and activated carbon from rice husk by leaching ash and chemical activation. Springerplus 2016;5(1):Article No. 1248.

Al-Asadi ST, Al-Qaim FF, Al-Saedi, HFS, Deyab IF, Kamyab H, Chelliapan S. Adsorption of methylene blue dye from aqueous solution using low-cost adsorbent: Kinetic, isotherm adsorption, and thermodynamic studies. Environmental Monitoring and Assessment 2023;195:Article No. 676

Al-Ghouti MA, Al-Absi RS. Mechanistic understanding of adsorption and thermodynamic aspects of cationic methylene blue dye onto cellulosic olive stones biomass from wastewater. Scientific Reports 2020;10:Article No. 15928.

Alau KK, Gimba CE, Agbaji BE, Abeche SE. Structural and microstructural properties of Neem husk and seed carbon activated with zinc chloride and phosphoric acid. Journal of Chemical and Pharmaceutical Research 2015;7(3):2470-9.

Amin MT, Alazba AA, Shafiq M. Effective adsorption of methylene blue dye using activated carbon developed from

rosemary plant: Isotherm and kinetic studies. Desalination and Water Treatment 2017;74:336-45.

Bakdash RS, Aljundi IH, Basheer C, Abdulazeez I. Rice husk derived Aminated Silica for the efficient adsorption of different gases. Scientific Reports 2020;10:Article No. 19526.

Banuprabha TR, Karthikeyan A, Kalyani P. Evaluation and application of phytomass derived activated carbons as electrodes for coin cell supercapacitors. International Journal of Electrochemical Science 2021;16:Article No. 211251.

Cychosz KA, Thommes M. Progress in the physisorption characterization of nanoporous gas storage materials. Engineering 2018;4:559-65.

El-Bindary MA, El-Desouky MG, El-Bindary AA. Adsorption of industrial dye from aqueous solutions onto thermally treated green adsorbent: A complete batch system evaluation. Journal of Molecular Liquids 2021;346:Article No. 117082.

El-Sayed GO, Yehia MM, Asaad AA. Assessment of activated carbon prepared from corncob by chemical activation with phosphoric acid. Water Resources and Industry 2014;7-8:66-75.

Faria PCC, Orfao JJM, Pereira MFR. Adsorption of anionic and cationic dyes on activated carbons with different surface chemistries. Water Research 2004;38(8):2043-52.

Han Q, Wang J, Goodman BA. High adsorption of methylene blue by activated carbon prepared from phosphoric acid treated eucalyptus residue. Powder Technology 2020;366:239-48.

Han X, Niu X, Ma X. Adsorption characteristics of methylene blue on poplar leaf in batch mode: Equilibrium, kinetics and thermodynamics. Korean Journal of Chemical Engineering 2012;107(3):494-502.

Hasani N, Selimi T, Mele A, Thaçi V, Halili J, Berisha A, et al. Theoretical, equilibrium, kinetics and thermodynamic investigations of methylene blue adsorption onto lignite coal. Molecules 2022;27(6):Article No. 1856.

Hazzaa R, Hussein M. Cationic dye removal by sugarcane bagasse activated carbon from aqueous solution. Global NEST Journal 2015;17(4):784-95.

Hongo T, Moriura M, Hatada Y, Abiko H. Simultaneous methylene blue adsorption and pH neutralization of contaminated water by rice husk ash. ACS Omega 2021;6:21604-12.

Horsfall Jnr M, Spiff AI. Effects o temperature on the sorption of $Pb^{2+}$and Cd^{2+} from aqueous solution by Caladium biochar (Wild Cocoyam) biomass. Electronic Journal of Biotechnology 2005;8(2):43-50.

Hossain SK S, Mathur L, Roy PK. Rice husk/rice husk ash as an alternative source of silica in ceramics: A review. Journal of Asian Ceramic Societies 2018;6(4):299-313.

Hu L, Yang Z, Wang Y, Li Y, Fan D, Wu D, et al. Facile preparation of water soluble hyperbranched polyamine functionalized multiwalled carbon nanotubes for high-efficiency organic dye removal room aqueous solution. Scientific Reports 2017;7(1):Article No. 3611.

Inglezakis VJ, Zorpas AA. Heat of adsorption, adsorption energy and activation energy in adsorption and ion exchange systems. Desalination and Water Treatment 2012;39:149-57.

Islam MA, Tan IAW, Benhouria A, Asif M, Hameed BH. Mesoporous and adsorptive properties of palm date seed activated carbon prepared via sequential hydrothermal carbonization and sodium hydroxide activation. Chemical Engineering Journal 2015;270:187-95.

İzgi MS, Saka C, Baytar O, Saraçoğlu G, Şahin Ö. Preparation and characterization of activated Carbon from microwave and conventional heated almond shells using phosphoric acid activation. Analytical Letters 2018;52(5):772-89.

Jawad AH, Rashid RM, Ismail K, Sabar S. High surface area mesoporous activated carbon developed from coconut leaf by chemical activation with H_3PO_4 for adsorption of methylene blue. Desalination and Water Treatment 2017;74:326-35.

Khuluk RH, Rahmat A, Buhani B, Suharso S. Removal of methylene blue by adsorption onto activated carbon from coconut shell (*Cocous Nucifera* L.). Indonesian Journal of Science and Technology 2019;4(2):229-40.

Kumar A, Jena HM. Preparation and characterization of high surface area activated carbon from *Fox nut* (Euryale ferox) shell by chemical activation with H_3PO_4. Results in Physics 2016;6:651-8.

Liu L, Deng G, Shi X. Adsorption characteristics and mechanism of p-nitrophenol by pine sawdust biochar samples produced at different pyrolysis temperatures. Scientific Reports 2020; 10:Article No. 5149.

Liu QS, Zheng T, Li N, Wang P, Abulikemu G. Modification of bamboo-based activated carbon using microwave radiation and its effects on the adsorption of methylene blue. Applied Surface Science 2010;256(10):3309-15.

Ma J, Yu F, Zhou L, Jin L, Yang M, Luan J, et al. Enhanced adsorptive removal of methyl orange and methylene blue from aqueous solution by alkali-activated multiwalled carbon nanotubes. ACS Applied Materials and Interfaces 2012; 4:5749-90.

Mansour RAE, Simeda MG, Zaatout AA. Removal of brilliant green dye from synthetic wastewater under batch mode using chemically activated date pit carbon. RSC Advances 2021;11:7851-61.

Patawat C, Silakate K, Chuan-Udom S, Supanchaiyamat N, Hunt AJ, Ngernyen Y. Preparation of activated carbon from *Dipterocarpus alatus* fruit and its application for methylene blue adsorption. RSC Advances 2020;10*:*21082-91.

Pathania D, Sharma S, Singh P. Removal of methylene blue by adsorption onto activated carbon developed from *Ficus carica* bast. Arabian Journal of Chemistry 2017;10(1):1445-51.

Puziy AM, Poddubnaya OI, Martınez-Alonso A, Suarez-Garcıa F, Tascon JMD. Synthetic carbons activated with phosphoric acid: I. Surface chemistry and ion binding properties. Carbon 2002;40(9):1493-505.

Serafin J, Dziejarski B, Junior OFC, Srenscek-Nazzal J. Design of highly microporous activated carbons based on walnut shell biomass for H_2 and CO_2 storage. Carbon 2023;201:633-47.

Sharma YC, Uma. Optimization of parameters for adsorption of methylene blue on a low-cost activated carbon. Journal of Chemical and Engineering Data 2010;55,435-9.

Shrestha LK, Thapa M, Shrestha RG, Maji S, Pradhananga RR, Ariga K. Rice husk-derived high surface area nanoporous carbon materials with excellent iodine and methylene blue adsorption properties. Journal of Carbon Research 2019;5(1):Article No. 10.

Thang NH, Khang DS, Hai TD, Nga DT, Tuan PD. Methylene blue adsorption mechanism of activated carbon synthesized from cashew nut shells. RSC Advances 2021;11:26563-70.

Tran HN, You S-J, Chao HP. Insight into adsorption mechanism of cationic dye onto agricultural residues-derived hydrochars: Negligible role of π-π interaction. Korean Journal of Chemical Engineering 2017;34(6):1708-20.

Uner O, Geçgl Ü, Bayrak Y. Adsorption of methylene blue by an efficient activated carbon prepared from *Citrullus lanatus*

rind: Kinetic, isotherm, thermodynamic, and mechanism analysis. Water, Air, and Soil Pollution 2016;227:Article No. 247.

Unugul T, Nigiz FU. Preparation and characterization an active carbon adsorbent from waste mandarin peel and determination of adsorption behavior on removal of synthetic dye solutions. Water, Air, and Soil Pollution 2020;231:Article No. 538.

Wantaneeyakul N, Kositkanawuth K, Turn SQ, Fu J. Investigation of biochar production from copyrolysis of rice husk and plastic. ACS Omega 2021;6(43):28890-902.

Wazir AH, Wazir IU, Wazir AM. Preparation and characterization of rice husk based physical activated carbon. Energy Sources, Part A: Recovery, Utilization, and Environmental Effects 2020;11:Article No. 1715512.

Wu FC, Liu BL, Wu KT, Tseng RL. A new linear form analysis of Redlich-Peterson isotherm equation for the adsorption of dyes. Chemical Engineering Journal 2010;162:21-7.

Xu L, Pan C, Li S, Yin C, Zhu J, Pan Y, et al. Electrostatic self-assembly synthesis of three-dimensional mesoporous lepidocrocite-type layered sodium titanate as a superior adsorbent for selective removal of cationic dyes via an ion-exchange mechanism. Langmuir 2021;37(19):6080-95.

Yakout SM, Sharaf El-Deen G. Characterization of activated carbon prepared by phosphoric acid activation of olive stones. Arabian Journal of Chemistry 2016;9(2):1155-62.

Zazouli MA, Azari A, Dehghan S, Salmani Malekkolae R. Adsorption of methylene blue from aqueous solution onto activated carbons developed from eucalyptus bark and *Crataegus oxyacantha* core. Water Science and Technology 2016;74(9):2021-35.

Zhu Y, Yi B, Yuan Q, Wu Y, Wang M, Yan S. Removal of methylene blue from aqueous solution by cattle manure derived low-temperature biochar. RSC Advances 2018; 8:19917-29.

Ziezio M, Charmas B, Jedynak K, Hawryluk M, Kucio K. Preparation and characterization of activated carbons obtained from the waste materials impregnated with phosphoric acid(V). Applied Nanoscience 2020;10:4703-16.